ORIGINAL SCIENTIFIC PAPER

CROATICA CHEMICA ACTA

Croat. Chem. Acta **2026**, *99*(2), 185–194
Published online: July 24, 2026
DOI: 10.5562/cca4249

HKD 1926

Reactivity and Intramolecular Interactions in Linalool: A Computational Study Using Reactivity Descriptors, NCI, NBO, and QTAIM Analyses

Karen Canseco-Sandoval, Clara Hilda Rios-Reyes, Luis Humberto Mendoza-Huizar*

Área Académica de Química, Universidad Autónoma del Estado de Hidalgo, carretera Pachuca–Tulancingo, 42184, Mineral de la Reforma, Hidalgo. México
* Corresponding author's e-mail address: hhuizar@uaeh.edu.mx

RECEIVED: December 23, 2025 ✯ REVISED: May 05, 2026 ✯ ACCEPTED: May 25, 2026

Abstract: In this study, the chemical reactivity of linalool was examined using global and local reactivity descriptors calculated at the X/6-311++G(2d,2p) level of theory (X = B3LYP, M06, M06L, ωB97XD, and MP2). The global reactivity indices indicate that linalool exhibits moderate electrophilic character. Fukui functions and frontier molecular orbital analysis identify C6 and C7 carbon atoms as the most reactive sites toward electrophilic and radical species, while nucleophiles preferentially interact with the hydrogen atom of the hydroxyl group and the hydrogen atoms attached to C5 and C6. Molecular electrostatic potential maps indicate that the hydroxyl group and the C6–C7 region are the most polarized regions of the molecule. Noncovalent interaction analysis suggests a weak intramolecular H–O···H–C interactions. However, Natural Bond Orbital (NBO) and Quantum Theory of Atoms in Molecules analyses show that this feature corresponds to a weak noncovalent contact rather than a conventional hydrogen bond. Also, NBO analysis indicates that the conformational stability of linalool is largely controlled by intramolecular hyperconjugative σ→σ* interactions along the carbon framework, enhanced by lone-pair donation from the hydroxyl oxygen.

Keywords: linalool, enantiomers, reactivity, fukui, MP2.

INTRODUCTION

LINALOOL is an acyclic monoterpene found extensively in a wide variety of aromatic plants.[1] This compound is a major fraction of the essential oils extracted from species such as *Lavandula angustifolia, Coriandrum sativum, Ocimum basilicum*, and *Cinnamomum zeylanicum*.[2] Due to its distinctive fragrance, linalool is widely employed in cosmetic, pharmaceutical, and food applications.[1] Linalool occurs in two enantiomeric forms, (3S)-3,7-dimethylocta-1,6-dien-3-ol (*S*) and (3R)-3,7-dimethylocta-1,6-dien-3-ol (*R*), which display pronounced differences in both odor perception and biological activity.[3] Sensory evaluations describe the *S* enantiomer as sweet and floral, while the *R* enantiomer possesses a predominantly woody aroma and occurs in oils including lavender.[4] Furthermore, the two linalool enantiomers exhibit distinct biological effects, manifested in variations in anticonvulsant activity,[5] stress response, and autonomic nervous system modulation.[6] Together, these differences suggest that molecular chirality is central to receptor binding and the activation of specific physiological pathways.[7,8] However, the underlying molecular mechanisms remain unclear. Therefore, evaluating the molecular reactivity of both *S* and *R* enantiomers may elucidate the interaction mechanisms associated with receptor activation.

Despite its broad industrial applications, linalool is a known fragrance allergen, primarily because its oxidation in air forms sensitizing species.[9] Prolonged contact with oxidized derivatives is linked to skin irritation and allergic responses, prompting interest in its intrinsic molecular reactivity. From a theoretical standpoint, analyzing linalool reactivity provides insight into its propensity for oxidation, establishing relationships between its electronic properties and allergenic behavior. Several investigations employing Density Functional Theory (DFT) have focused on characterizing both the global and site-specific reactivity of linalool.[10] Khadom et al.,[11] using the B3LYP/6–31G(d,p) level, found that electrophilic species preferentially interact with the C7 and C8 positions, while C2 and O are the

This work is licensed under a Creative Commons Attribution 4.0 International License.

most reactive toward nucleophilic attack; for free radicals, C6 and C7 were identified as the most vulnerable sites. In contrast, Wu et al.,[12] employing the same functional with the 6–31G(d) basis set, identified O and C5 as the most reactive centers toward electrophiles and C7 and C8 as the most vulnerable to nucleophiles. Likewise, Laihmedi et al.,[13] reported that atoms C7 and C8 are the most likely sites for electrophilic attack, while C2 and C3 are the most probable for nucleophilic attack. Such inconsistencies highlight the dependence of predicted local reactivity on the chosen level of theory and basis set. Additionally, conformational mobility and conjugated π-systems can significantly influence electronic distribution, affecting reactivity descriptors. Notably, these studies do not explicitly specify the enantiomeric form considered. In this study, the MP2 method is incorporated as a benchmark to evaluate the robustness of DFT predictions and the role of electron correlation. The analysis determines global (μ, η, χ, ω and $\Delta\omega$) and local (Fukui functions) descriptors to identify molecular regions prone to electrophilic, nucleophilic, and radical interactions, clarifying the degree of agreement among the computational approaches.

THEORY

Conceptual Density Functional Theory provides a quantitative framework for describing molecular reactivity through a set of well-defined descriptors. Within this theoretical approach, both global and local reactivity descriptors can be derived, enabling a quantitative assessment of the electronic stability, charge-transfer tendencies, and the electron-accepting or electron-donating capacity of a molecule. Among the main global descriptors are the chemical potential (μ), electronegativity (χ), chemical hardness (η), and the global electrophilicity index (ω), defined by the following expressions:[14]

$$\mu = \left(\frac{\partial E}{\partial N}\right)_{v(r)} = \frac{1}{2}(I + A) \quad (1)$$

$$\chi = -\mu \quad (2)$$

$$\eta = \left(\frac{\partial \mu}{\partial N}\right)_{v(r)} = \left(\frac{\partial^2 E}{\partial N^2}\right)_{v(r)} \frac{1}{2}(I - A) \quad (3)$$

$$\omega = \frac{\mu^2}{2\eta} \quad (4)$$

In these equations, N represents the number of electrons, E the total energy of the system, and $v(r)$ the external potential generated by the nuclei. The terms I and A correspond to the ionization potential and the electron affinity, respectively. μ is related to the ease with which a system can release electronic charge;[14,15] its negative value is associated with greater system stability. χ defined as the negative of the chemical potential, measures the ability of a system to attract electrons.[14,15] η quantifies the resistance of the system to changes in its electron density and is therefore associated with the intrinsic stability of the molecule.[14,15] On the other hand, ω describes the predisposition of a system to accept electronic charge; larger ω values correspond to systems with enhanced electron-accepting capability, whereas low values characterize good electron donors.[16] Based on this index, the parameters of electroaccepting power (ω^+) and electrodonating power (ω^-) are also defined, which allow a more detailed differentiation of the system's behavior in charge-transfer processes:[16]

$$\omega^- = \frac{(\mu^-)^2}{2\eta} = \frac{\left(-\frac{1}{4}(3I + A)\right)^2}{2(I - A)} \quad (5)$$

$$\omega^+ = \frac{(\mu^+)^2}{2\eta} = \frac{\left(-\frac{1}{4}(I + 3A)\right)^2}{2(I - A)} \quad (6)$$

Additionally, the difference

$$\Delta\omega = \omega^+ - \omega^- \quad (1)$$

is defined, which corresponds to the nucleophilicity of the system. Positive values of $\Delta\omega$ indicate that the system has a stronger electron-donating (nucleophilic) character, whereas negative values indicate a greater tendency to accept electronic charge (electrophilic character).

While global descriptors allow the interpretation of a molecule's average reactivity, it is necessary to use local descriptors to identify the specific sites where chemical interactions occur. A particularly informative local descriptor is the Fukui function (f(r)), originally formulated within conceptual DFT,[17] it is defined as the derivative of the electron density with respect to the number of electrons at a constant external potential:

$$f(r) = \left(\frac{\partial \rho(r)}{\partial N}\right)_{v(r)} = \left(\frac{\partial \mu(r)}{\partial v(r)}\right) \quad (8)$$

Through this descriptor, spatial regions with enhanced susceptibility toward different types of chemical attack can be distinguished to electrophilic ($f^-(r)$), nucleophilic ($f^+(r)$), or radical ($f^0(r)$) attacks. There are different methods for its calculation, including the frozen-core approximation, the finite difference method, and

atomic charges. Under the frozen-core approximation, the Fukui function is evaluated directly from the densities of the frontier orbitals, Eqs. (9)–(11):[17]

$$f^{-}(r) = \varphi^{*}_{H}(r)\varphi_{H}(r) = \rho_{H}(r) \quad (9)$$

$$f^{+}(r) = \varphi^{*}_{L}(r)\varphi_{L}(r) = \rho_{L}(r) \quad (10)$$

$$f^{0}(r) = \frac{1}{2}\left(\rho_{H}(r) + \rho_{L}(r)\right) \quad (11)$$

Where $\rho_H(r)$ and $\rho_L(r)$ represent the electron densities of the HOMO and LUMO, respectively. On the other hand, using the finite difference method, the Fukui function is obtained from the electron densities of the neutral ($\rho_N(r)$), cationic ($\rho_{N-1}(r)$), and anionic ($\rho_{N+1}(r)$) species, according to Eqs. (12–14):[17]

$$f^{-}(r) = \rho_{N}(r) - \rho_{N-1}(r) \quad (12)$$

$$f^{+}(r) = \rho_{N+1}(r) - \rho_{N}(r) \quad (13)$$

$$f^{0}(r) = \frac{1}{2}\left(\rho_{N+1}(r) - \rho_{N-1}(r)\right) \quad (14)$$

Alternatively, by using atomic charges instead of densities, the local Fukui functions (FFs) for atom j are expressed as Eqs. (15)–(17):[18]

$$f_j^{-}(r) = q_{j(N-1)} - q_{j(N)} \quad (15)$$

$$f_j^{+}(r) = q_{j(N)} - q_{j(N+1)}(r) \quad (16)$$

$$f^{0}(r) = \frac{1}{2}\left(q_{j(N-1)} - q_{j(N+1)}\right) \quad (17)$$

Where q_j represents the atomic charge obtained through a charge partitioning scheme. These functions allow the identification of the atoms in linalool that are most susceptible to participating in specific chemical reactions, providing a quantitative description of their local reactivity, complementary to the global analysis.

METHODS

Initial molecular geometry coordinates for (*S*)-linalool (PubChem CID 67179) and (*R*)-linalool (PubChem CID 443158) were obtained from the PubChem database. To identify the global minimum energy structure, we performed an extensive random conformational search using HyperChem software.[19] The torsional space was explored via the MM+ force field, executing 1,000 iterations per enantiomer to ensure exhaustive sampling of the aliphatic chain's rotational degrees of freedom. Each randomly generated structure underwent full geometry optimization, with duplicate structures filtered according to atomic distance criteria. An energy window of 0.1 kcal mol^{-1} was applied for conformer selection, identifying the geometry with the lowest potential energy as the most stable conformer for subsequent analyses. Full geometry optimizations in the aqueous phase were performed using four DFT functionals: B3LYP,[20] M06,[21] M06L,[22] and ωB97XD,[23] with the 6–311++G(2d, 2p) basis set.[24–26] This basis set includes diffuse and polarization functions for accurately describing electron density and noncovalent interactions. ωB97XD was employed to account for dispersion and long-range effects, while M06 and M06L evaluated meta–GGA contributions to molecular reactivity. B3LYP served as a reference due to its widespread application in organic systems. Solvent effects were modeled using the polarizable continuum model (PCM).[27,28] Vibrational frequency analyses confirmed that all DFT optimized structures correspond to energy minima on the potential energy surface. MP2 (second-order Møller–Plesset perturbation theory) was employed as a reference, wavefunction-based method to complement the DFT calculations.[29] MP2 explicitly accounts for electron correlation, providing an independent assessment of electronic structure and intramolecular interactions.[30] This approach is particularly useful for validating DFT results in systems where dispersion and weak non-covalent interactions are significant.[31] Although MP2 has known limitations, including sensitivity to basis set size and occasional underestimation of electron affinities, it serves as a reliable benchmark to confirm trends observed with DFT, thus MP2 results are reported as reference.[32] Noncovalent Interaction (NCI) analysis was conducted to visualize and quantify weak intramolecular interactions, including hydrogen bonds and van der Waals interactions.[33] Natural Bond Orbital (NBO) analysis was performed to gain insight into donor–acceptor interactions and to estimate stabilization energies associated with intramolecular charge–transfer effects.[34,35] In addition, the Quantum Theory of Atoms in Molecules (QTAIM) method was employed to confirm the existence of interactions, characterize the type of bonding, and analyze the topological structure of the electron density.[36] All quantum calculations were carried out using Gaussian 09,[37] and visualized with GaussView,[38] Avogadro,[39] and Multiwfn.[40]

RESULTS AND DISCUSSION

The conformational search based on PubChem structures (CID 67179 and CID 443158) yielded two non–superimposable mirror-image geometries corresponding to the *S* and *R*

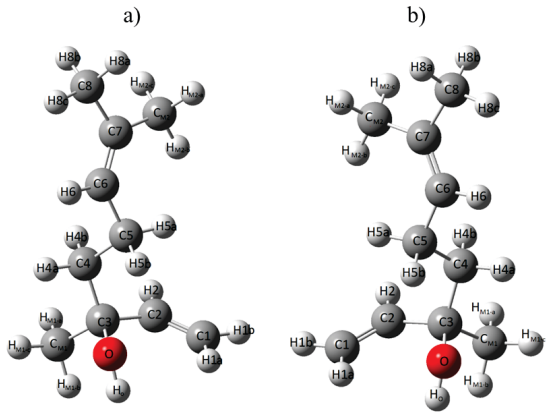


Figure 1. Enantiomers of linalool: a) (3*S*)–3,7–dimethylocta-1,6–dien-3-ol (*S*) and b) (3*R*)–3,7-dimethylocta–1,6–dien–3–ol (*R*) optimized at the MP2/6–311++G(2d,2p) level of theory. $d_{C1–C2}$= 1.337 Å, $d_{C2–C3}$= 1.506 Å, $d_{C3–C4}$= 1.53 Å, $d_{C4–C5}$= 1.531 Å, $d_{C5–C6}$= 1.502 Å, $d_{C6–C7}$= 1.345 Å, $d_{C7–C8}$= 1.505 Å, $d_{C3–CM1}$= 1.527 Å, $d_{C3–CM1}$= 1.504 Å, dihedral angle (C1–C2–C3–O) = –1.215°, dihedral angle (C5–C6–C7–C_{M2})=-0.924°, dihedral angle (C2–C3–C4–C5)=–61.115°. *xyz* coordinates are given as Supporting Information in Table S1.

enantiomers. Since the conformational freedom of linalool is equivalent for both enantiomers, they exhibit the same number of accessible conformers within the conformational space. Furthermore, each conformer of the *S* enantiomer has a corresponding mirror-image counterpart in the *R* enantiomer. From an electronic structure perspective, enantiomeric structures possess identical global and local descriptors when evaluated in the absence of chiral fields or external perturbations. These structures were optimized using the B3LYP, M06, M06L, and ωB97XD functionals with the 6-311++G(2d, 2p) basis set. Subsequent vibrational frequency analyses yielded exclusively positive frequencies, confirming that the structures represent genuine minima on the potential energy surface. Starting from the DFT–optimized geometries, unconstrained optimizations were performed at the MP2/6–311++G(2d, 2p) level (Figure 1). Identical bond distances, angles, and dihedral angles were obtained for both enantiomers. The XYZ coordinates for the *S* and *R* enantiomers are provided in the Supporting Information (Table S1).

Global Reactivity Descriptors

Global reactivity descriptors for linalool enantiomers were evaluated using the B3LYP, M06, M06L, and ωB97XD functionals with the 6-311++G(2d, 2p) basis set, with MP2 calculations serving as a reference (Table 1). The values of ionization potential and electron affinity are reported in Table S2 of the Supporting Information. Consistent with theoretical expectations, no differences were observed in the global descriptor values between the *R* and *S* enantiomers, confirming that stereochemistry does not affect the intrinsic global reactivity of isolated linalool enantiomers. The calculated electronegativity (χ) and chemical potentials (μ) indicate that B3LYP and M06 yield slightly more negative values (approx –3.6 eV) than M06L, ωB97XD, and MP2, suggesting a greater propensity for charge–transfer processes. In contrast, MP2 yields a less negative μ value, reflecting a more conservative description of the electronic distribution. A similar pattern emerges for the electrophilicity index (ω), where B3LYP and M06 produce the highest values (approx 2.2 eV), while ωB97XD and MP2 predict lower electrophilicity. Chemical hardness (η) varies significantly across methods, ranging from 2.60 eV (MP2) to 3.16 eV (ωB97XD). The higher hardness predicted by ωB97XD reflects greater resistance to electronic deformation, whereas the lower values from B3LYP and MP2 indicate a higher capacity for charge redistribution. The electron-donating (ω^+) and electron-accepting (ω^-) powers follow a consistent trend. In all cases, the electron-accepting power is considerably larger than the electron-donating power, demonstrating that linalool is more prone to accept electronic charge. $\Delta\omega$ further reflects the disparity between donor and acceptor behavior. In general, despite quantitative variations among the computational approaches, all methods characterize linalool as a moderately electrophilic molecule with a primary tendency to accept electrons.

Table 1. Global reactivity descriptors for *S* and *R* linalool enantiomers evaluated at the MP2/6-311++G(2d, 2p) level of theory in the aqueous phase according to Eqs.(1)–(7).

	μ / eV	η / eV	χ/ eV	ω / eV	ω^+ / eV	ω^- / eV	$\Delta\omega$ / eV
B3LYP	–3.604	2.846	3.604	2.282	0.836	4.440	–3.604
M06	–3.577	2.886	3.577	2.218	0.790	4.366	–3.576
M06L	–3.307	2.947	3.307	1.856	0.570	3.878	–3.308
ωB97XD	–3.338	3.159	3.338	1.764	0.490	3.826	–3.336
MP2	–2.584	2.604	2.584	1.282	0.316	2.900	–2.584

Local Reactivity Descriptors

Local reactivity was evaluated using FFs, identifying molecular regions preferentially involved in nucleophilic, electrophilic, and radical attacks. Within the frozen-core approximation, FFs are interpreted via frontier molecular orbitals (HOMO and LUMO) according to Eqs. (9–11), providing insights into electron density localization and reactive behavior. Figure 2 shows the frontier orbital distributions for the *S* enantiomer at the MP2/6-311++G(2d, 2p) level; equivalent distributions were obtained for the *R* enantiomer. Complementary results for B3LYP, M06, M06L, and ωB97XD are provided in Table S3 (Supporting Information). Analysis reveals that the HOMO is concentrated on the C6=C7 double bond (Figure 2a), identifying this region as the most susceptible to electrophilic attack, with additional contributions from C5, C8, and the C7–methyl group. Notably, HOMO patterns remain consistent across all functionals (Table S3), indicating minimal dependence on the exchange–correlation treatment. In contrast, the LUMO of the *S* enantiomer at the MP2/6-311++G(2d, 2p) level (Figure 2b) shows dominant electron density at C1, C2, and the methyl groups at C3 and C7, suggesting these sites are more susceptible to nucleophilic attack. The LUMO distribution exhibits a stronger functional dependence (Table S3 of the Supporting Information). Only the ωB97XD results reproduce the MP2 LUMO distributions, whereas B3LYP, M06, and M06L display noticeable spatial variations. This behavior reflects the intrinsic sensitivity of virtual orbitals to the treatment of long-range exchange and dispersion interactions. Finally, radical attack susceptibility was evaluated using Eq. (11) at the MP2/6-311++G(2d, 2p) level (Figure 2c), identifying C6, C7, C5, and C8 as the most reactive sites. Similar trends were observed with B3LYP, M06, M06L, and ωB97XD (Table S3 of the Supporting Information).

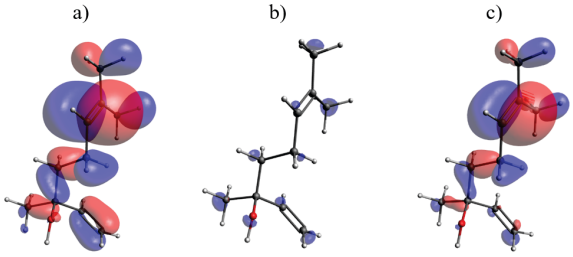


Figure 2. HOMO and LUMO distributions of the *S* enantiomer, obtained at the MP2/6-311++G(2d, 2p) level of theory in the aqueous phase using the PCM solvation model, for (a) electrophilic, (b) nucleophilic, and (c) free radical attacks, calculated according to Eqs. (9)–(11). In all cases, the isosurfaces were generated at an isovalue of 0.02 e/Å³.

Also, FFs were computed via the finite-difference approximation at the MP2/6-311++G(2d, 2p) level according to Eqs. (12)–(14) (Figure 3). For both enantiomers, electrophilic and radical reactivity (f^- and f^0) are primarily localized at the C6 and C7 alkene carbons (Figures 3a and 3c), identifying this double bond as the most favorable site for electrophilic and radical attack. In contrast, nucleophilic reactivity (f^+) is distributed across C4, C5, and C6 (Figure 3b). The same spatial distribution was observed for the *R* enantiomer, aligning with the theoretical expectation that enantiomers possess identical intrinsic electronic properties in achiral environments. Also, FFs were calculated using the B3LYP, M06, M06L, and ωB97XD functionals to analyze their influence on the prediction of local reactivity, see Table S4 (Supporting information). All functionals identify C6 and C7 as the primary electrophilic and radical centers, demonstrating consistent predictions for f^-. However, the nucleophilic Fukui function (f^+) exhibits significant functional dependence. Among the functionals considered, only ωB97X–D reproduces the nucleophilic sites predicted by MP2. This agreement stems from the range-separated scheme in ωB97X–D, which incorporates a larger fraction of Hartree–Fock exchange at long interelectronic distances and an empirical dispersion correction. These features mitigate electron delocalization errors, ensuring a more accurate description of long-range interactions. Since f^+ strongly depends on the LUMO character and the density change upon electron addition, ωB97X-D provides a more reliable prediction of nucleophilic reactive sites, consistent with the MP2 results.

Condensed Fukui functions (CFFs) were calculated using Eqs. (15)–(17) to provide a localized and quantitative description of atomic reactivity. The indices were derived from Hirshfeld atomic populations, a partitioning scheme that typically yields positive Fukui values, facilitating their interpretation.[41,42] Table 2 summarizes the condensed Fukui indices for electrophilic, nucleophilic, and radical

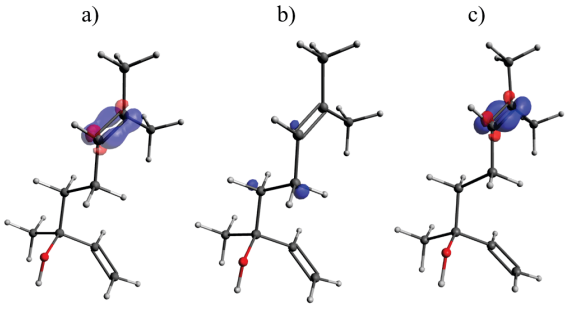


Figure 3. Fukui function isosurfaces (ρ = 0.01 e Å^{-3}) for the S enantiomer, calculated according to Eqs. (12)–(14) at the MP2/6–311++G(2d, 2p) level of theory using the PCM solvation model. (a) electrophilic, (b) nucleophilic, and (c) free radical attacks.

Table 2. Fukui function values for electrophilic attacks (f^-(r)), nucleophilic attacks (f^+(r)), and radical attacks (f^0(r)) in the *S* and *R* enantiomers. Atomic labeling corresponds to the numbering shown in Figure 1. Cn and Hn refer to the atoms of the main skeleton; Hna/Hnb/Hnc indicate non-equivalent hydrogens attached to the same carbon; and labels such as C_{M1} and C_{M2} identify the carbons of the methyl substituents bonded to C3 and C7.

Atom	f^-	f^+	f^0
C1	0.010	0.041	0.025
H1a	0.005	0.050	0.027
H1b	0.003	0.041	0.022
C2	–0.003	0.020	0.008
H2	0.002	0.047	0.025
C3	0.005	0.009	0.007
C_{M1}	0.004	0.022	0.013
$H_{M1–a}$	0.003	0.036	0.019
$H_{M1–b}$	0.006	0.020	0.013
$H_{M1–c}$	0.003	0.032	0.018
O	0.004	0.027	0.015
H_O	0.005	0.054	0.030
C4	0.015	0.021	0.018
H4a	0.013	0.029	0.021
H4b	0.014	0.049	0.032
C5	0.026	0.033	0.029
H5a	0.022	0.025	0.024
H5b	0.032	0.084	0.058
C6	0.242	0.036	0.139
H6	0.074	0.067	0.070
C7	0.213	0.018	0.115
C_{M2}	0.037	0.036	0.036
$H_{M2–a}$	0.023	0.036	0.029
$H_{M2–b}$	0.041	0.042	0.042
$H_{M2–c}$	0.044	0.036	0.040
C8	0.040	0.019	0.030
H8a	0.044	0.019	0.031
H8b	0.044	0.016	0.030
H8c	0.028	0.027	0.028

attacks for the S enantiomer at the MP2/6–311++G(2d, 2p) level; equivalent atoms in the R enantiomer display identical values. The results indicate that the highest electrophilic susceptibility (f^-) occurs at carbons C6 (0.242) and C7 (0.213), corresponding to the C=C double bond. These atoms also exhibit the largest radical indices (f^0), identifying the alkene region as the primary reactive center for both electrophilic and radical species. In contrast, the largest nucleophilic indices (f^+) are associated with aliphatic hydrogens, specifically H5b (0.084), H6 (0.067), and the hydroxyl hydrogen (HO, 0.054). This distribution suggests that these positions act as the primary sites for nucleophilic interaction, whereas the alkene moiety is the most favorable region for electrophiles or radicals. The nucleophilic indices are more widely distributed among hydrogen atoms bonded to saturated carbons, reflecting polarization effects and local charge redistribution along the carbon framework. The Fukui function values for the *S* and *R* enantiomers, calculated at the X/6–311++G(2d, 2p) level of theory (B3LYP, M06, M06L, and ωB97XD), are reported in Table S5 of the Supporting information.

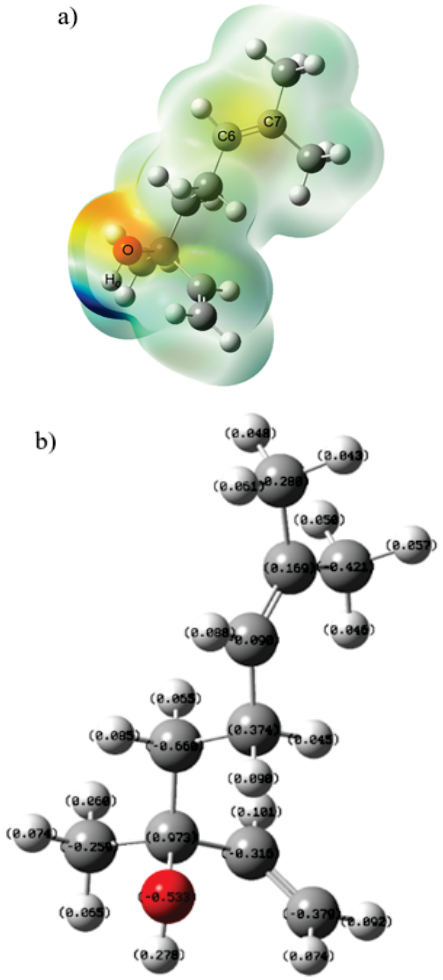


Figure 4. Mapping of electrostatic potentials evaluated on a density isosurface (ρ = 0.002 e/Å^3) at the MP2/6–311++G(2d, 2p) level of theory using the PCM solvation model. (b) Mulliken population analysis.

Molecular Electrostatic Potential Maps and Charge Distribution

Molecular electrostatic potential (MEP) maps provide complementary insights into reactivity by depicting the spatial distribution of potential over the molecular surface. Figure 4a illustrates the MEP map for the *S* enantiomer. In this representation, red regions correspond to negative electrostatic potential (high electron density), while blue regions indicate positive potential (electron-deficient zones). For both enantiomers, the potential extrema are located at the hydroxyl group bonded to C3. The oxygen atom exhibits the most negative potential, consistent with its high electronegativity, whereas the hydroxyl hydrogen presents the most positive potential, reflecting its electropositive character. A second region of negative potential is observed at the C6–C7 double bond, aligning with the reactive sites identified via Fukui and condensed Fukui function analyses. The molecular charge distribution (Figure 4b) is consistent with the MEP map and the optimized structures display a dipole moment of 2.3898 D. Collectively, the MEP results confirm that the alkene and hydroxyl groups constitute the primary reactive regions, which are electronically equivalent in both *S* and *R* enantiomers.

Analysis of Non–covalent Interactions

Regions characterized by a near-zero reduced density gradient (RDG) were analyzed using the Noncovalent Interaction (NCI) approach [Eq. (18)]. In the RDG versus sign(λ_2)$\rho(r)$ plot (Figure 5) for the *S* enantiomer, negative values correspond to attractive interactions, while positive values indicate repulsive or steric regions.[33]

$$s(r) = \frac{1}{2(2\pi^2)^{1/3}} \frac{|\nabla\rho(r)|}{\rho(r)^{4/3}} \quad (18)$$

The reliability of NCI analysis depends on the basis set and the treatment of electron correlation; therefore, calculations were performed at the MP2/6–311++G(2d, 2p) level. The RDG–sign(λ_2)(r) scatter plot displays characteristic peaks at –0.0025, –0.010, –0.012, –0.014, 0.0025, 0.010, 0.012, and 0.014. The most negative regions (between –0.012 and –0.014) correspond to stabilizing intramolecular interactions, specifically weak H–O···H–C interactions type. Less negative regions (–0.01 to –0.0025) indicate weak dispersive interactions, such as H···H interactions. Conversely, positive values (0.0025–0.014) reflect steric repulsion arising from the proximity of methyl and methylene groups, which suggest that conformational stability is primarily directed by these weak noncovalent interactions. Figure 6 illustrates the NCI isosurfaces, where red regions indicate steric repulsion, and green-to-blue surfaces correspond to dispersive and hydrogen-bonding-like

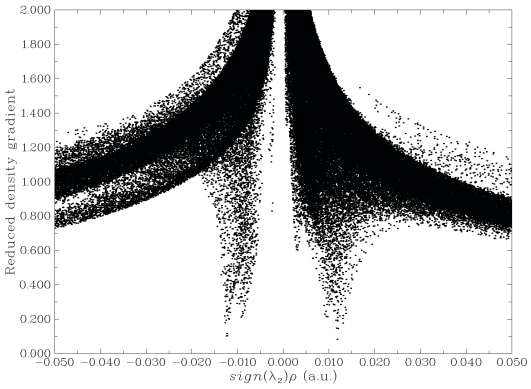


Figure 5. Plot of the reduced density gradient (RDG) versus sign(λ_2)ρ for the *S* enantiomer in the aqueous phase, calculated at the MP2/6–311++G(2d, 2p) level of theory.

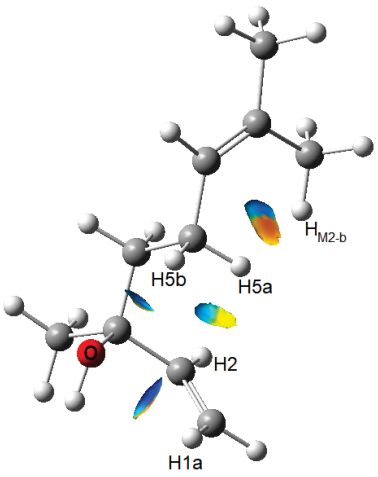


Figure 6. NCI isosurface (s = 0.8 e Å^{-3}) for the *S* enantiomer in the aqueous phase, calculated at the MP2/6–311++G (2d, 2p) level of theory.

interactions. These findings align with the RDG plots and confirm the role of dispersion in determining conformational preferences. The hydroxyl group orientation promotes a weak intramolecular interaction, resulting in a more compact and stabilized conformation. Equivalent results were obtained for the *R* enantiomer.

Natural Bond Orbital, (NBO) Analysis

Donor–acceptor interactions in the S enantiomer of linalool were analyzed using second-order perturbation theory within the Natural Bond Orbital (NBO) framework to quantify intramolecular charge transfer and stabilization energies.[34,35] For each donor (*i*) and acceptor (*j*) orbital, $E(2)$ was calculated according to Eq. (19), where qi is the donor occupancy, E_i and E_j are orbital energies, and $F(i,j)$

represents the Fock matrix element describing orbital coupling.

$$E(2) = \Delta E_{ij} = q_i \frac{F(i,j)^2}{E_i - E_j} \quad (19)$$

The most significant donor → acceptor interactions and their associated stabilization energies are summarized in Table 3. The NBO analysis suggests that stabilization is primarily directed by hyperconjugative σ→σ* interactions along the carbon skeleton, along with lone-pair donation from the hydroxyl oxygen. The strongest interactions include σ(C–H) → σ*(C–C) hyperconjugation, such as BD C6–H6 → BD* C7–CM2 (~ 9 kcal·mol^{-1}), as well BD C1–H1b → BD* C3–C2 and BD C_{M1}–$H_{M1\text{-}a}$ → BD* C3–O (~ 6–7 kcal·mol^{-1}). σ(C–C) → σ*(C–C) interactions contribute moderately (4–5 kcal·mol^{-1}) to electronic flexibility and conformational stability. Lone-pair donation from oxygen, specifically LP(2) O → BD* C3–C2 (~ 8.6 kcal·mol^{-1}), further stabilizes the molecular framework. Notably, while NCI analysis identifies an O···H1a interaction, NBO analysis reveals no significant donor–acceptor contact, indicating negligible orbital overlap and electronic stabilization. Consequently, the stability of the *S* enantiomer arises from cooperative σ→σ* hyperconjugation and oxygen lone-pair donation, highlighting the role of intramolecular charge transfer in conformational stabilization. The same conclusions were drawn for the *R* enantiomer.

Quantum Theory of Atoms in Molecules (QTAIM) Analysis

The electronic structure of the *S* and *R* enantiomers was further investigated via topological analysis of the electron density using Bader's Quantum Theory of Atoms in Molecules (QTAIM),[36] to characterize the nature and strength of intramolecular interactions.[43] Bond critical points (BCPs) were identified, see Figure 7, and the electron density ($\rho(r_c)$) and its Laplacian ($\nabla^2\rho(r_c)$) were evaluated at these points; numerical values are reported in Table S6 of the Supporting information. Most critical points (1–19 and 22) display negative ($\nabla^2\rho(r_c)$) values, indicating electron density concentration in the internuclear region and interactions of predominantly covalent character, with varying strengths reflected in $\rho(r_c)$, see Table S6. In contrast, critical points 20, 21 and 23–29 exhibit positive Laplacian values. Specifically, critical point 25 exhibits a positive Laplacian ($\nabla^2\rho(r_c)$ = 0.025412 a.u.) and a low electron density ($\rho(r_c)$ = 0.008451 a.u.), these values identify a closed-shell interaction, characteristic of weak noncovalent interactions. Notably, the NCI analysis reveals reduced density gradient regions between the oxygen atom and nearby hydrogen atoms, indicating the presence of weak H-O···H-C interactions. In particular, RDG isosurfaces appear for the H-O···H1a and H-O···H5b interactions at distances of 2.51 and 2.55 Å, respectively (see Figure 6). However, no bond critical points were identified in these regions within the framework of the QTAIM. This absence indicates that the electron density between these atoms is too diffuse and weak to establish a classical hydrogen bond; the interactions do not meet the QTAIM criteria for hydrogen bonding, which typically require a localized electron density region connecting the donor and acceptor atoms. For comparison reasons and in order to quantitatively characterize these regions in the absence of BCPs, the electronic properties were evaluated at the local minima of the RDG (s_{min}),[33] and these points were selected as the most representative of the interaction, as they correspond to the valley where the gradient is minimal, serving as the closest physical analogue to a BCP in weak or disperse contacts.[44] The exact spatial coordinates of these smin points were identified using Multiwfn,[40] through a high-resolution grid search (0.03 Bohr step size) to ensure the convergence and numerical stability of the located minima. Electronic properties were then calculated via point-evaluation to maintain consistency with the BCP data in Table S6, allowing for a direct numerical comparison of interaction magnitudes. At these points, the sign of the second eigenvalue of the Hessian ($\lambda_2 < 0$) was verified to confirm the attractive nature of the contacts. The H-O···H1a interaction exhibits an electron density ($\rho(r)$ = 0.015 a.u.) and a positive Laplacian ($\nabla^2\rho(r)$ = 0.0771 a.u.), consistent with a weak, closed-shell contact. In contrast, the H-O···H5b

Table 3. Some table. Width: 455.4 points

Donor NBO (*i*)	Acceptor NBO (*j*)	*E*(2) / kcal·mol^{-1}	*E*(*j*)–*E*(*i*) / a.u.	*F*(*i*,*j*) / a.u.	Interpretation
BD (1) C6–H6	BD*(1) C7–CM2	9.18	1.64	0.089	Strong σ(C–H) → σ*(C–C) hyperconjugation involving the methyl substituent
LP (2) O	BD*(1) C3–C2	8.57	0.86	0.079	Lone pair donation n(O) → σ*(C–C) from the hydroxyl oxygen
BD (1) C1–H1b	BD*(1) C3–C2	6.79	1.53	0.088	σ(C–H) → σ*(C–C) hyperconjugative stabilization
BD CM1–HM1-a	BD*(1) C3–O	6.37	1.32	0.084	σ(C–H) → σ*(C–O) interaction near the hydroxyl group

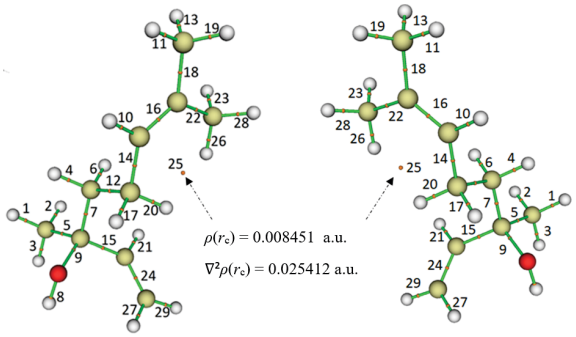


Figure 7. Molecular graph of the *S* and *R* enantiomers obtained at the MP2/6-311++G(2d,2p) level of theory. Small orange spheres indicate the bond critical points (BCPs) identified by QTAIM analysis.

contact shows a lower electron density ($\rho(r)$ = 0.0120 a.u.) and a positive Laplacian ($\nabla^2\rho(r)$ = 0.0549 a.u.), indicating a relatively weaker attractive interaction compared to the former. Consequently, these results demonstrate the presence of weak H–O···H–C interactions of varying strengths. Although the electron density and Laplacian values at the RDG local minima fall within the typical ranges for hydrogen bonding, the absence of a BCP confirms that these interactions do not fulfill the formal topological requirements of a hydrogen bond. Instead, they represent diffuse non-covalent interactions where the electron density fails to consolidate into a discrete bonding pathway.

CONCLUSIONS

In this work, it was found that the reactivity descriptors indicate that both linalool enantiomers act as moderate electrophiles and exhibit nearly identical global electronic properties. Furthermore, local reactivity analyses, based on Fukui functions, frontier molecular orbitals, and condensed indices, indicate that the C6 and C7 alkene carbons constitute the main sites susceptible to electrophilic and radical attack, while nucleophilic interactions are mainly associated with the hydrogen of the hydroxyl group and with aliphatic hydrogens located at C5 and C6. The NCI analysis suggests the possible presence of an H–O···H–C hydrogen-bond–type interaction; however, NBO and QTAIM analyses confirm that this feature corresponds to a weak noncovalent interaction rather than a stabilized intramolecular hydrogen bond.

Acknowledgment. KCS, CHRR and LHMH thankfully acknowledges the computer resources, technical expertise, and support provided by the Laboratorio Nacional de Supercómputo del Sureste de México, CONACYT member of the network of national laboratories through the project No 202501011N. The Guanajuato National Laboratory (CONACyT 123732) is gratefully acknowledged for providing supercomputing resources. LHMH acknowledges the Universidad Autónoma del Estado de Hidalgo for the support granted to carry out this work. LHMH also thanks the SNII for the recognition of his membership and the financial stipend received.

Supplementary Information. Supporting information to the paper is attached to the electronic version of the article at: https://doi.org/10.5562/cca4249.

PDF files with attached documents are best viewed with Adobe Acrobat Reader which is free and can be downloaded from Adobe's web site.

REFERENCES

[1] Y. Bueno-Duarte, S. C. Mendez-Sanchez, *Vitae (Medellín)*. **2015**, *22*, 33–41. https://doi.org/10.17533/udea.vitae.v22n1a04

[2] V. De Moura, A. Lourenc, M. Figueiro, L. Piato, A. Paula, F. Dupont, D. Sa, P. Roberto, H. Moreno, E. Elisabetsky, *Phytomedicine*. **2009**, *16*, 303–307. https://doi.org/10.1016/j.phymed.2008.08.001

[3] R. E. Sonstrom, D. M. Cannon, J. L. Neill, *Symmetry (Basel).* **2022**, *14*, 917. https://doi.org/10.3390/sym14050917

[4] W. Mączka, A. Duda-Madej, M. Grabarczyk, K. Wińska, *Molecules*. **2022**, *27*, 6928. https://doi.org/10.3390/molecules27206928

[5] D. de Sousa, F. Nóbrega, C. Santos, R. de Almeida, *Nat Prod Commun*. **2010**, *5* (12), 1847–1851. https://doi.org/10.1177/1934578X1000501201

[6] N. Yamamoto, S. Fujiwara, K. Saito-Iizumi, A. Kamei, F. Shinozaki, Y. Watanabe, K. Abe, A. Nakamura, *Biosci. Biotechnol. Biochem.* **2013**, *77* , 2413–2418. https://doi.org/10.1271/bbb.130524

[7] M. Höferl, S. Krist, G. Buchbauer, *Planta Med.* **2006**, *72* , 1188–1192. https://doi.org/10.1055/s-2006-947202

[8] K. Weston-Green, H. Clunas, C. Jimenez Naranjo, *Front. Psychiatry*. **2021**, *12*, 1–19. https://doi.org/10.3389/fpsyt.2021.583211

[9] Z. Yi, J. Chen, L. Yong, C. Zhou, Y. Yuan, Y. Li, *J. AOAC Int.* **2022**, *105* , 1576–1584. https://doi.org/10.1093/jaoacint/qsac093

[10] H. Manzoor, M. U. Khan, S. Khan, M. Shah, C. A. Shabbir, H. M. Alkhtani, *PLoS One*. **2025**, *20* , e0325281. https://doi.org/10.1371/journal.pone.0325281.

[11] A. A. Khadom, M. M. Kadhim, R. A. Anaee, H. B. Mahood, M. S. Mahdi, A. W. Salman, *J. Mol. Liq.* **2021**, *343*, 116978. https://doi.org/10.1016/j.molliq.2021.116978.

[12] K. Wu, Y. Lin, X. Chai, X. Duan, X. Zhao, C. Chun, *Food Sci. Nutr.* **2019**, *7* , 2546–2555. https://doi.org/10.1002/fsn3.1104
[13] F. Laihmedi, A. Barhoumi, B. Lizoul, K. Mounich, T. Benabbouha, M. Chafi, A. Zeroial, M. E. Idrissi, *Turkish Comput. Theor. Chem.* **2023**, *8* , 13–22. https://doi.org/10.33435/tcandtc.1286725
[14] R. G. Parr, W. Yang, *Density-Functional Theory of Atoms and Molecules*, First ed., Oxford University Press, New York **1989**.
[15] R. Pal, P. K. Chattaraj, *J. Indian Chem. Soc.* **2021**, *98* , 100008. https://doi.org/10.1016/j.jics.2021.100008
[16] R. G. Parr, L. V. Szentpály, S. Liu, *J. Am. Chem. Soc.* **1999**, *121* , 1922–1924. https://doi.org/10.1021/ja983494x
[17] R. G. Parr, W. Yang, *J. Am. Chem. Soc.* **1984**, *106*, 4049–4050. https://doi.org/10.1021/ja00326a036
[18] W. Yang, W. J. Mortier, *J. Am. Chem. Soc.* **1986**, *108*, 5708–5711. https://doi.org/10.1021/ja00279a008
[19] Hypercube, Inc. *HyperChem Professional 8.0*; Hypercube, Inc.: Gainesville, FL, USA**, 2011.**
[20] K. Raghavachari, *Theor. Chem. Accounts 2000 1033*. **2000**, *103*, 361–363. https://doi.org/10.1007/s002149900065
[21] Y. Zhao, D. G. Truhlar, *Theor. Chem. Acc.* **2008**, *120* (1–3), 215–241. https://doi.org/10.1007/s00214-007-0310-x
[22] Y. Wang, X. Jin, H. S. Yu, D. G. Truhlar, X. He, *Proc. Natl. Acad. Sci. U. S. A.* **2017**, *114*, 8487–8492. https://doi.org/10.1073/pnas.1705670114
[23] J. Da Chai, M. Head-Gordon, *Phys. Chem. Chem. Phys.* **2008**, *10* , 6615–6620. https://doi.org/10.1039/b810189b
[24] R. Krishnan, J. S. Binkley, R. Seeger, J. A. Pople, *J. Chem. Phys.* **1980**, *72*, 650–654. https://doi.org/10.1063/1.438955
[25] A. D. McLean, G. S. Chandler, *J. Chem. Phys.* **1980**, *72*, 5639–5648. https://doi.org/10.1063/1.438980
[26] W. L. Jorgensen, J. Chandrasekhar, J. D. Madura, R. W. Impey, M. L. Klein, *J. Chem. Phys.* **1983**, *79*, 926–935. https://doi.org/10.1063/1.445869
[27] S. Miertuš, E. Scrocco, J. Tomasi, *Chem. Phys.* **1981**, *55*, 117–129. https://doi.org/10.1016/0301-0104(81)85090-2
[28] S. Miertuš, J. Tomasi, *Chem. Phys.* **1982**, *65*, 239–245. https://doi.org/10.1016/0301-0104(82)85072-6
[29] R. A. Mata, M. A. Suhm, *Angew. Chemie - Int. Ed.* **2017**, *56*, 11011–11018. https://doi.org/10.1002/anie.201611308
[30] S. Grimme, C. Muck-Lichtenfeld, J. Antony, *Phys. Chem. Chem. Phys.* **2008**, *10*, 3318–3319. https://doi.org/10.1039/b808067b
[31] K. E. Riley, J. A. Platts, J. Řezáč, P. Hobza, J. G. Hill, *J. Phys. Chem. A*. **2012**, *116*, 4159–4169. https://doi.org/10.1021/jp211997b
[32] T. Benighaus, R. A. Distasio, J. R. C. Lochan, J. Da Chai, M. Head-Gordon, *J. Phys. Chem. A*. **2008**, *112*, 2702–2712. https://doi.org/10.1021/jp710439w
[33] E. R. Johnson, S. Keinan, P. Mori-Sánchez, J. Contreras-García, A. J. Cohen, W. Yang, *J. Am. Chem. Soc.* **2010**, *132*, 6498–506. https://doi.org/10.1021/ja100936w
[34] E. D. Glendenning, A. E. Reed, J. E. Carpenter, F. Weinhold, *NBO Version 3.1*, **1998**.
[35] C. Karthika, R. Praveena, S. Ramachandran, K. Sadasivam, G. Salgado, P. Muñoz, L. Gerli, L. H. Mendoza-Huizar, *Croat. Chem. Acta*. **2020**, *93*, 147–155. https://doi.org/10.5562/cca3695
[36] R. F. W. Bader, Atoms in Molecules: A Quantum Theory, Oxford University Press, Oxford University Press. **1990**.
[37] M. J. Frisch, G. W. Trucks, H. B. Schlegel, G. E. Scuseria, M. A. Robb, J. R. Cheeseman, G. Scalmani, V. Barone, B. Mennucci, G. A. Petersson, et al., **2009**.
[38] J. M. Dennington, R. D.; Keith, T. A. & Millam, **2008**.
[39] M. D. Hanwell, D. E. Curtis, D. C. Lonie, T. Vandermeerschd, E. Zurek, G. R. Hutchison, *J. Cheminform.* **2012**, *4*, 1–17. https://doi.org/10.1186/1758-2946-4-17
[40] T. Lu, F. Chen, *J. Comput. Chem.* **2012**, *33*, 580–592. https://doi.org/10.1002/jcc.22885
[41] F. L. Hirshfeld, *Theor. Chim. Acta*. **1977**, *44*, 129–138. https://doi.org/10.1007/BF00549096
[42] P. K. Chattaraj, *Chemical Reactivity Theory : A Density Functional View*, CRC Press/Taylor & Francis **2009**. https://doi.org/10.1201/9781420065442
[43] D. Shilpa, K. Sadasivam, L. H. Mendoza-Huizar, *Dokl. Phys. Chem.* **2024**, *517*, 96–112. https://doi.org/10.1134/S0012501625600032
[44] G. Saleh, C. Gatti, L. Lo Presti, J. Contreras-Garcia, *Chem. - A Eur. J.* **2012**, *18*, 15523–15536. https://doi.org/10.1002/chem.201201290